

Waveform Optimization and Beam Focusing for Near-field Wireless Power Transfer with Dynamic Metasurface Antennas and Non-linear Energy Harvesters

Amirhossein Azarbahram, *Graduate Student Member, IEEE*, Onel L. A. López, *Member, IEEE*,
and Matti Latva-Aho, *Fellow, IEEE*

Abstract—Radio frequency (RF) wireless power transfer (WPT) is a promising technology for future wireless systems. However, the low power transfer efficiency (PTE) is a critical challenge for practical implementations. One of the main inefficiency sources is the power consumption and loss introduced by key components such as high-power amplifier (HPA) and rectenna, thus they must be carefully considered for PTE optimization. Herein, we consider a near-field RF-WPT system with the emerging dynamic metasurface antenna (DMA) at the transmitter and non-linear energy harvesters. We provide a mathematical framework to calculate the power consumption and harvested power from multi-tone signal transmissions. Then, we propose an approach relying on alternating optimization and successive convex approximation for waveform optimization and beam focusing to minimize power consumption while meeting energy harvesting requirements. Numerical results show that increasing the transmit tones reduces the power consumption by leveraging the rectifier’s non-linearity. Moreover, it is demonstrated that increasing the antenna length improves the performance, while both DMA and fully-digital architectures may be favorable depending on the setup. Finally, our results verify that the transmitter generates accurate energy beams pointed to devices located in the near-field, while energy beams are formed in devices’ direction in the far-field region.

Index Terms—Radio frequency wireless power transfer, waveform design, beamforming, dynamic metasurface antennas, near-field channels.

I. INTRODUCTION

FUTURE wireless systems will facilitate efficient and eco-friendly communication across a myriad of low-power devices, fostering a sustainable society. Achieving this requires uninterrupted connectivity among these devices and with the underlying infrastructure, all while mitigating disruptions arising from battery depletion [1]–[3]. This is potentially facilitated by energy harvesting (EH) technologies providing wireless charging, thus, easing the maintenance of Internet of Things (IoT) devices and increasing their lifespan. Moreover, EH may lead to improved energy efficiency and reduced emission footprints across the network [4].

EH receivers may harvest energy from two types of sources: those that exist in the surrounding environment, and those that

A. Azarbahram, O. López and M. Latva-Aho are with Centre for Wireless Communications (CWC), University of Oulu, Finland, (e-mail: {amirhossein.azarbahram, onel.alcarazlopez, matti.latva-aho}@oulu.fi).

This work is partially supported in Finland by the Finnish Foundation for Technology Promotion, Academy of Finland (Grants 348515 and 346208 (6G Flagship)), the Finnish-American Research and Innovation Accelerator, and by the European Commission through the Horizon Europe/JU SNS project Hexa-X-II (Grant Agreement no. 101095759).

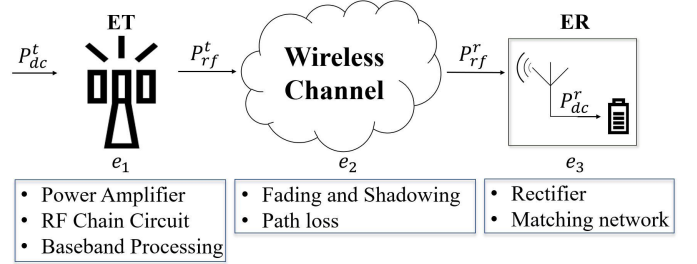


Fig. 1: Block diagram of a typical WPT system. The power consumption and loss sources are listed under each block.

are specifically designated for energy transmission. From a transmission perspective, the latter is supported by wireless power transfer (WPT) technologies, e.g., based on inductive coupling, magnetic resonance coupling, laser power beaming, and radio frequency (RF) radiation. Among them, RF-WPT is promising for charging multiple users relatively far from the transmitter by exploiting the broadcast nature of wireless channels. Furthermore, this can be accomplished over the same infrastructure used for wireless communications. Notably, the most important challenge toward maturing RF-WPT is related to increasing the inherently low end-to-end power transfer efficiency (PTE) [4]. Herein, we focus on RF-WPT, which is referred to as WPT in the following.

A. Preliminaries

The end-to-end PTE depends on the performance of the key building blocks, namely energy transmitter (ET), wireless channel, and energy receiver (ER) as illustrated in Fig. 1. At first, a signal is generated and amplified using a direct current (DC) power source at the ET. Then, it is upconverted to the RF domain and transmitted over the wireless channel. Finally, the ER converts the received RF signal to DC for EH purposes. Indeed, the end-to-end PTE comprises: DC-to-RF, RF-to-RF, and RF-to-DC power conversion efficiency, i.e.,

$$e = \underbrace{\frac{P_{rf}^t}{P_{dc}^t}}_{e_1} \times \underbrace{\frac{P_{rf}^r}{P_{rf}^t}}_{e_2} \times \underbrace{\frac{P_{dc}^r}{P_{rf}^r}}_{e_3} = \frac{P_{dc}^r}{P_{dc}^t}. \quad (1)$$

In WPT, both transmitter and receiver introduce non-linearities to the signals affecting the amount of harvested power. Indeed, an appropriately designed transmit signal leveraging these non-linearities may reduce the power consumption at the transmitter and/or increases the RF-to-DC conversion efficiency

at the receiver [5], [6]. Specifically, using multiple transmit frequency tones can lead to high peak-to-average power ratio (PAPR) signals at the receiver, enhancing the rectifier RF-to-DC conversion efficiency [7]. Meanwhile, the RF signal can be focused towards the ER using energy beamforming (EB), which affects the transmit/receive waveform, to cope with the channel inefficiencies captured by e_2 , thereby enhancing the amount of RF power that can be harvested [4]. Notice that the active transmit components consume power to operate, while the passive elements introduce power losses, both of which impact e_1 and must be considered. Therefore, e_1 , e_2 , and e_3 are correlated, suggesting that their joint optimization may lead to significant gains in terms of end-to-end PTE.

The end-to-end PTE is also affected by the system power consumption. One of the main factors contributing greatly to the power consumption is the transmitter's architecture, which also determines the beamforming approach. For example, in a fully-digital structure, each antenna element necessitates a dedicated RF chain, with its corresponding high-power amplifier (HPA), consuming a significant amount of power. An HPA aims to amplify the input signal to compensate for the path loss and fading in a wireless system. Moreover, the signal amplification in the HPA requires a DC power source, which accounts for the majority of the power consumption. The significant drawback of the fully-digital architecture is the high complexity and cost, making it impractical for applications requiring massive multiple-input multiple-output (mMIMO) implementations. Alternatively, analog architectures using, e.g., passive phase shifters, are less expensive but offer limited degrees of freedom for EB. Thus, a hybrid architecture implementation combining both approaches is often more appealing in practice. Hybrid architectures offer a trade-off between complexity (cost) and beamforming flexibility [8], [9].

Although hybrid beamforming using phase shifters promotes cost reduction, it still requires complex analog networks for phase shifting. There are emerging technologies to provide hybrid beamforming capability with an even lower cost and complexity, e.g., reflective intelligent surface (RIS)-aided systems [10] and dynamic metasurface antennas (DMAs) [11]. Notice that RIS is an assisting node that provides the passive beamforming capability using reflective elements, while DMA is a transceiver consisting of configurable metamaterial elements and a limited number of RF chains. DMA avoids analog network implementation challenges and provides hybrid beamforming capability with low cost and complexity. Each of these architectures may be favorable based on the system setup. For instance, employing multiple low-cost RISs helps to cover the blind spots that are prone to weak signal reception in a large area. However, reflecting surfaces in RIS-assisted systems lack baseband processing capability to perform channel estimation and send pilot signals. Thus, acquiring accurate enough channel state information to attain a suitable passive beamforming gain might force huge overheads to the system [12]. On the other hand, DMA is a transceiver and has sufficient baseband processing capability for channel estimation. However, its implementation requires some RF chains making it more costly than RIS for large-scale implementation. All in all, both of these architectures

support low-cost transmitter deployments, while the choice highly depends on the considered system setup. Interestingly, the authors in [13] utilize a system model comprising both RIS and DMA structures for uplink MIMO communication, while assuming that the channel is perfectly known.

B. Prior works

There are many works either focusing on EB, waveform optimization, or joint waveform and beamforming design for fully-digital WPT systems. The authors in [14] utilize EB to power multiple devices in a MIMO system consisting of radio stripes, while the deployment problem of this transmit architecture is investigated in [15]. Furthermore, a low-complexity beamforming design relying on the statistics of the channel is proposed in [16] to fairly power a set of single-antenna devices. In the mentioned works, none of the practical system non-linearities are considered and the focus is on the received RF power at the devices. In [17], transmit beamforming and RF and DC combining at the receiver are leveraged to increase the received DC power in a MIMO WPT system. Although this work considers the rectifier's non-linearity, the waveform design is not investigated. Moreover, a low-complexity waveform design for single-user setups is proposed in [18], while the large-scale multi-antenna WPT scenario is addressed in [19]. The authors in [20] leverage beamforming and a multi-sine waveform in a MIMO WPT system to enhance the harvested power. Notably, the frameworks in [18]–[20] consider the rectifier non-linearity. Interestingly, the authors in [21] perform waveform and beamforming optimization while considering both main non-linearity sources (HPA and rectifier) aiming to maximize the harvested DC power in a WPT system.

Although most of the works on WPT systems in the literature focus on traditional fully-digital architecture, novel low-cost transmitters have also attained significant attention recently. For instance, DMA is utilized in [22], [23] for a near-field WPT system, while the authors in [24] propose a minimum-power beamforming design for meeting quality of service requirements of the users in a simultaneous wireless information and power transfer (SWIPT) system. However, none of these studies have considered the rectifier non-linearity and its impact on the harvested DC power. Notably, the joint waveform and beamforming design problem in RIS-aided WPT and SWIPT systems is investigated in [25] and [26], respectively. Furthermore, the two latter works consider the EH non-linearity at the receiver side, thus, taking into account its impact on the harvested DC power.

C. Contributions

All in all, WPT systems have received considerable attention for some time. Still, more effort is needed to reduce the system power consumption, thus increasing the end-to-end PTE. For this, low-cost multi-antenna transmitters like DMA are appealing and may pave the way for charging devices efficiently in massive IoT deployments. Moreover, multiple studies aimed to enhance the amount of harvested DC power (with rectifier non-linearity) in far-field WPT systems or received RF power (without rectifier non-linearity) in near-field WPT. As mentioned before, the receiver does not perform RF-to-DC conversion linearly and the shape of the waveform may

leverage the receiver’s RF-to-DC conversion efficiency. Thus, it is imperative to take into account the impact of the rectifier’s non-linearity in the system. To the best of our knowledge, no work has yet investigated the radiative near-field power transmission and the power consumption of a multi-antenna WPT system for meeting the EH requirements of a multi-user setup while considering the receiver non-linearity, especially when using low-cost transmitters. Herein, we aim precisely to fill this research gap. Our main contributions are as follows:

1) We formulate a joint waveform optimization and beam focusing problem for a multi-user multi-antenna WPT system with both a fully-digital and a DMA architecture. Due to the huge potential of near-field WPT systems for future practical WPT applications [3], we present our system model relying on a near-field wireless channel, which can inherently capture far-field conditions as well. Notice that there are some previous works [21], [25], which focused on increasing the amount of harvested power in far-field WPT systems while considering the receiver non-linearity. However, the literature lacks a minimum-power waveform and beamforming design (even for far-field channels), which can deal with meeting the EH requirements. This is a critical gap to fill since such formulation mimics a practical setup where the EH users inform their DC power demands and the WPT system must serve them with minimum power consumption, thus maximum end-to-end PTE. Since the HPA is an active element incurring most of the power consumption at the transmitter side, we model the power consumption of a class-B HPA as a function of its output power. Notably, our problem for fully-digital architecture shares some similarities with the one discussed in [21] as objectives and constraints are interchanged. However, the main focus of our work here is on the DMA-assisted system, which introduces much more complexity to the problem due to the coupling between the variables and their Lorentzian-constrained phase response. Note that the phase shift introduced by the metamaterial elements is correlated with their amplitude, which results in a different beamforming problem than other architectures, e.g., RIS-assisted systems [26] and phase shifter-based hybrid beamforming [9]. Mathematically, when dealing with those latter architectures, both RIS passive elements or phase shifters introduce a phase shift to the signal with constant loss¹, while each phase-shifting configuration in DMA elements leads to a different propagation loss introduced to the transmit signal. The complexities associated with our specific problem make the existing optimization frameworks for WPT systems inapplicable to our system calling for novel approaches.

2) We propose a method relying on alternating optimization and successive convex approximation (SCA) to efficiently solve the waveform and beamforming optimization problem in the DMA-assisted WPT system. Specifically, we decouple the optimization problem to maximize the minimum received DC power by tuning the frequency response of the metamaterial elements, while minimizing the consumed power for meeting the EH requirements when optimizing the digital precoders.

¹Note that in most of the works in the literature, without loss of generality, this phase shifting process by the analog network or RIS elements is considered to be lossless.

Generally, a huge complexity is introduced to the waveform optimization problems by time sampling since the number of samples should be relatively large to result in a reliable framework [6], [20], [21]. To cope with this, we reformulate the received DC power of the users based on the spectrum of the received waveform, which removes the time dependency in the problem. Then, the metamaterial elements and the digital precoders are alternatively optimized using SCA. Motivated by the influence of variable initialization on the SCA performance, we propose a low-complexity initialization algorithm for the digital precoders and DMA weights by leveraging the channel characteristics and dedicating RF signals to the ERs. Furthermore, the complexity of the proposed optimization framework scales with the number of users, antenna elements, and frequency tones.

3) We illustrate the convergence of the proposed optimization method numerically and show that the complexity increases with the antenna length, number of transmit tones, and number of devices. Furthermore, we provide evidence that increasing the antenna length and the number of transmit tones reduces power consumption, while it increases with the number of devices and user distance. Moreover, our findings evince that DMA performs better in terms of power consumption when the number of RF chains and transmit tones are relatively low, while the fully-digital architecture becomes favorable when the mentioned parameters are sufficiently large. This also depends on the specific HPAs’ saturation power, number of devices, and user distance. Additionally, we verify by simulation that the transmitter can accurately focus the energy on the receiver location in the near-field region, while energy beams are only formed toward specific directions in the far-field region.

The remainder of the paper is structured as follows. Section II introduces the system model, including the transmit architectures, and signal and power consumption modeling. The optimization problem for a joint waveform and beamforming design, together with the proposed solving approach, are elaborated in Section III. Section IV discusses the proposed initialization algorithm, Section V presents the numerical results, while Section VI concludes the paper.

Notations: Bold lower-case letters represent column vectors, while non-boldface characters refer to scalars, $\mathbf{a} \odot \mathbf{b}$ denotes the Hadamard product of \mathbf{a} and \mathbf{b} , and $\{x\}$ is a set that contains x . The l_2 -norm of a vector is denoted as $|\cdot|$. The mathematical expectation is represented by \mathbb{E} and $(\cdot)^T$ and $(\cdot)^*$ are used to indicate the transpose and conjugate of a matrix or vector, respectively. Furthermore, the real and the imaginary parts of a complex number are denoted by $\Re\{\cdot\}$ and $\Im\{\cdot\}$, respectively. Additionally, $\lfloor \cdot \rfloor$ is the floor operator, and $\langle \cdot \rangle$ denotes the phase of a complex number.

II. SYSTEM MODEL

We consider a multi-antenna WPT system to charge M single-antenna EH devices. The received RF power at the ER is transferred into the rectifier input using a matching network. Then, it is converted to DC power by the rectifier, while P_m denotes the EH requirement of the m th ER.

As previously mentioned, multi-tone waveforms can be exploited to leverage the rectifier non-linearity and achieve a better end-to-end PTE. Hence, we consider multi-tone signals with N_f tones at frequencies f_1, f_2, \dots, f_{N_f} for power transmission purposes. Without loss of generality, we set $f_n = f_1 + (n-1)\Delta_f$, $n = 1, \dots, N_f$, where f_1 and Δ_f are the lowest sub-carrier frequency and the sub-carrier spacing, respectively.

A. Transmit Antenna Architectures

The transmitter is equipped with a uniform planar array (UPA) and $N_{rf} \geq M$ RF chains. The radiating elements are spaced uniformly, with N_h and N_v being the number of elements in the horizontal and vertical direction, respectively. Thus, the total number of elements is $N = N_v \times N_h$. Two types of transmit antenna architectures are considered: 1) Fully-digital architecture, which requires a dedicated RF chain for each radiating element, thus $N_{rf} = N$, as shown in Fig. 2a. In a fully-digital architecture, there is a single-stage beamforming process. Herein, $\omega_{i,n}$ is the complex weight of the n th frequency tone of the i th multi-tone waveform. Despite the high deployment cost and complexity, a fully-digital structure offers the highest number of degrees of freedom in beamforming.

2) DMA-assisted architecture, which comprises N_v waveguides, each fed by a dedicated RF chain and composed of N_h configurable metamaterial elements. Therefore, the number of RF chains, and consequently the cost and complexity, is considerably reduced compared to digital structures, making DMA suitable for mMIMO applications. Notice that DMA-assisted systems employ a two-stage beamforming process, i.e., digital beamforming, followed by the tuning of the amplitude/phase variations introduced by the metamaterial elements, as illustrated in Fig. 2b. Herein, $q_{i,l}$ is the tunable frequency response of the l th metamaterial element in the i th waveguide, while $h_{i,l}$ is the corresponding waveguide propagation loss, which will be explained in detail later.

B. Channel Model

In wireless communications, the region where the users are located between the Fraunhofer and Fresnel distances denoted respectively as d_{fr} and d_{fs} , is the radiative near-field region, which is referred to as the near-field region in the following. Specifically, a device at distance r from a transmitter experiences near-field conditions if $\sqrt{\frac{D^4}{8\lambda_1}} = d_{fs} < d < d_{fr} = \frac{2D^2}{\lambda_1}$, where D is the antenna diameter, i.e., the largest size of the antenna aperture, $\lambda_1 = \frac{c}{f_1}$ is the corresponding wavelength to the system operating frequency, and c is the speed of light. Notice that both system frequency and antenna form factor influence the region of operation. Therefore, by moving toward higher frequencies, e.g., millimeter wave and sub-THz bands, and/or utilizing larger antenna arrays, the far-field communication assumption regarding planar wavefronts may not be valid anymore. Instead, wavefronts impinging a receive node may be strictly spherical, thus, with advanced capabilities to focus the transmit signals on specific spatial points rather than on spatial directions.

Notice that one of the main applications of WPT systems is in indoor environments with line-of-sight (LOS) and near-field

communication, e.g., restaurants, warehouses, and shopping malls. Thus, we employ the near-field LOS channel model described in [27]. The Cartesian coordinate of the l th radiating element in the i th row is $\mathbf{g}_{i,l} = [x_{i,l}, y_{i,l}, z_{i,l}]^T$. Additionally, $i = 1, 2, \dots, N_v$ and $l = 1, 2, \dots, N_h$. The channel coefficient between user m and the l th element in the i th row at the n th sub-carrier is given by

$$\gamma_{i,l,m,n} = A_{i,l,m,n} e^{-\frac{j2\pi}{\lambda_n} d_{i,l,m}}, \quad (2)$$

where $\frac{2\pi}{\lambda_n} d_{i,l,m}$ is the phase shift caused by the propagation distance of the n th tone, with wavelength λ_n , and $d_{i,l,m} = |\mathbf{g}_m - \mathbf{g}_{i,l}|$ is the Euclidean distance between the element and the user located at \mathbf{g}_m . Moreover,

$$A_{i,l,m,n} = \sqrt{F(\Theta_{i,l,m})} \frac{\lambda_n}{4\pi d_{i,l,m}} \quad (3)$$

is the corresponding channel gain coefficient. Here, $\Theta_{i,l,m} = (\theta_{i,l,m}, \psi_{i,l,m})$ is the elevation-azimuth angle pair, and $F(\Theta_{i,l,m})$ is the radiation profile of each element. In addition, we employ the radiation profile as presented in [28], where

$$F(\Theta_{i,l,m}) = \begin{cases} G_t \cos(\theta_{i,l,m})^{\frac{G_t}{2}-1}, & \theta_{i,l,m} \in [0, \pi/2], \\ 0, & \text{otherwise,} \end{cases} \quad (4)$$

$G_t = 2(b+1)$ is the transmit antenna gain, and b denotes the boresight gain, which depends on the specifications of the antenna elements. Note that the channel coefficient becomes $A_m e^{-j\psi_{i,l,m}}$ for far-field communication, where A_m only depends on the distance of the user m from the transmitter and $\psi_{i,l,m}$ is solely determined by the user direction and the relative disposition of the antenna elements within the array.

C. Transmit & Receive Signals

The signal at the input of the i th HPA is given by

$$x_i(t) = \sum_{n=1}^{N_f} \omega_{i,n} e^{j2\pi f_n t}, \quad i = 1, \dots, N_{rf}. \quad (5)$$

The HPA introduces signal distortion and models such as the Rapp model [29] capture this non-linearity. It is shown in [21] that when the HPA operates in the non-linear regime, choosing a single-carrier waveform is preferred to a multi-carrier one. The reason is that a single-carrier waveform is less deteriorated by the adverse effect of the signal distortion caused by the HPA when operating in the non-linear regime. On the other hand, when HPAs operate in the linear regime, thus, not causing amplitude and phase distortion in the signal, multi-carrier waveforms are preferred since they leverage the rectifier's non-linearity and enhance the harvested power performance.

Note that the non-linear regime of the HPA happens near the saturation voltage. Thus, in practice, the HPAs can be properly chosen to have a suitable value of the saturation voltage based on the system setup and avoid operation in the non-linear regime. Since the aim of this work is to design multi-carrier waveforms for DMA-assisted WPT, we consider HPAs to operate in the linear regime. Mathematically, the output signal of the HPA is modeled as $x_i^{hpa}(t) = Gx_i(t)$, where G is the HPA gain. The rest of the signal modeling formulation will be presented separately for different transmit architectures in the following.

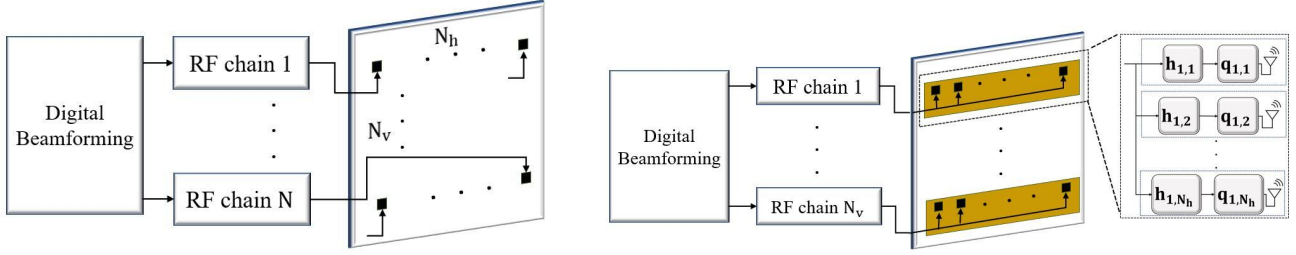


Fig. 2: Transmit antenna architectures. (a) fully-digital architecture (left) (b) DMA-assisted architecture (right).

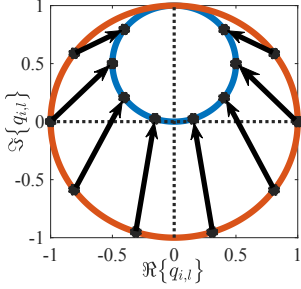


Fig. 3: The Lorentzian constrained (the inner circle) and the ideal weights (outer circle) in the complex plane. The arrows depict the mapping between the weights.

1) *Fully-Digital Architecture*: Herein, $N_{rf} = N$, thus, the real transmit signal at the output of the l th element in the i th row of the UPA can be expressed as

$$x_{i,l}^{FD}(t) = \Re\left\{x_{u(i,l)}^{hpa}(t)\right\} = G \sum_{n=1}^{N_f} \Re\left\{\omega_{u(i,l),n} e^{j2\pi f_n t}\right\}, \quad (6)$$

where $u(i, l) = (i - 1)N_h + l$. Thereby, the RF signal at the m th receiver when exploiting the fully-digital architecture can be expressed as

$$y_m^{FD}(t) = \sum_{i=1}^{N_v} \sum_{l=1}^{N_h} \sum_{n=1}^{N_f} \gamma_{i,l,m,n} x_{i,l}^{FD}(t) = G \sum_{i=1}^{N_v} \sum_{l=1}^{N_h} \sum_{n=1}^{N_f} \Re\left\{\gamma_{i,l,m,n} \omega_{u(i,l),n} e^{j2\pi f_n t}\right\}. \quad (7)$$

Furthermore, by defining $\mathbf{w}_n = [\omega_{1,n}, \dots, \omega_{N,n}]^T$ and $\boldsymbol{\gamma}_{m,n} = [\gamma_{m,n,1,1}, \gamma_{m,n,1,2}, \dots, \gamma_{m,n,N_v,N_h}]^T$, (7) can be reformulated as

$$y_m^{FD}(t) = G \sum_{n=1}^{N_f} \Re\left\{\boldsymbol{\gamma}_{m,n}^T \mathbf{w}_n e^{j2\pi f_n t}\right\}. \quad (8)$$

2) *DMA-assisted Architecture*: In metasurface antennas, the phase and amplitude that can be configured in the radiating elements are correlated due to the Lorentzian resonance. Herein, we capture this correlation by [30]

$$q_{i,l} \in \mathcal{Q} = \left\{(j + e^{j\phi_{i,l}})/2 \mid \phi_{i,l} \in [0, 2\pi]\right\}, \quad \forall i, l. \quad (9)$$

where $\phi_{i,l}$ are the tunable phase of the l th metamaterial element in the i th waveguide. As shown in Fig. 3, the ideal phase shifting exhibits a constant unit amplitude, i.e., no

losses, while the amplitude of the Lorentzian weights depends on the configured phase.

Herein, microstrip lines are used as waveguides, similar to [27], [31]. The propagation model of the signal within a microstrip is expressed as $h_{i,l} = e^{-(l-1)d_l(\alpha_i + j\beta_i)}$, where d_l is the inter-element distance, α_i represents the waveguide attenuation coefficient, and β_i is the propagation constant. The mathematical model of the DMA is represented in Fig. 2b.

Notice that the number of RF chains in the DMA is reduced to $N_{rf} = N_v$. Hence, the real transmit signal radiated from the l th element in the i th microstrip can be expressed as

$$x_{i,l}^{DMA}(t) = G \Re\left\{h_{i,l} q_{i,l} x_i^{hpa}(t)\right\} = G \sum_{n=1}^{N_f} \Re\left\{h_{i,l} q_{i,l} \omega_{i,n} e^{j2\pi f_n t}\right\}. \quad (10)$$

Furthermore, the RF signal received at the m th user in the DMA-assisted system is given by

$$y_m^{DMA}(t) = \sum_{i=1}^{N_v} \sum_{l=1}^{N_h} \sum_{n=1}^{N_f} \gamma_{i,l,m,n} x_{i,l}^{DMA}(t) = G \sum_{i=1}^{N_v} \sum_{l=1}^{N_h} \sum_{n=1}^{N_f} \Re\left\{\gamma_{i,l,m,n} h_{i,l} q_{i,l} \omega_{i,n} e^{j2\pi f_n t}\right\}. \quad (11)$$

Finally, we define

$$\bar{\mathbf{w}}_n = \underbrace{[\omega_{1,n}, \dots, \omega_{1,n}]}_{N_h}, \dots, \underbrace{[\omega_{N_v,n}, \dots, \omega_{N_v,n}]}_{N_h}^T \in \mathbb{C}^{N \times 1},$$

$\mathbf{q} = [q_{1,1}, \dots, q_{N_v,N_h}]^T$, $\mathbf{h} = [h_{1,1}, \dots, h_{N_v,N_h}]^T$, and reformulate (11) as

$$y_m^{DMA}(t) = G \sum_{n=1}^{N_f} \Re\left\{(\boldsymbol{\gamma}_{m,n} \odot \mathbf{q} \odot \mathbf{h})^T \bar{\mathbf{w}}_n e^{j2\pi f_n t}\right\}. \quad (12)$$

D. Rectenna

At the receiver side, the RF signal is converted to DC. This can be modeled by an antenna equivalent circuit and a single diode rectifier as illustrated in Fig. 4. The RF signal at the input of the antenna is denoted as $y_m(t)$ and has an average power of $\mathbb{E}\{y_m(t)^2\}$. Let us denote the input impedance of the rectifier and the impedance of the antenna equivalent circuit by R_{in} and R_{ant} , respectively. Thus, assuming perfect matching ($R_{in} = R_{ant}$), the input voltage at the rectifier of the m th ER

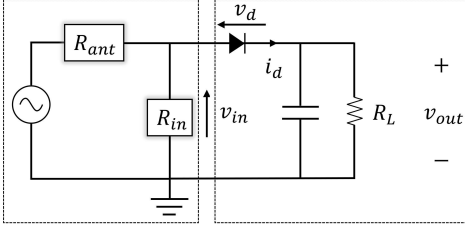


Fig. 4: Antenna equivalent circuit (left) and a single diode rectifier (right) [20].

is given by $v_{in,m}(t) = y_m(t)\sqrt{R_{ant}}$. Furthermore, the diode current can be formulated as

$$i_d(t) = i_s \left(e^{\frac{v_d(t)}{\hat{n}v_t}} - 1 \right), \quad (13)$$

where i_s is the reverse bias saturation current, \hat{n} is the ideality factor, v_t is the thermal voltage, and $v_d(t) = v_{in}(t) - v_o(t)$ is the diode voltage. Moreover, $v_{o,m}(t)$ is the output voltage of the m th rectifier, which can be approximated utilizing the Taylor expansion as [19], [20]

$$v_{o,m} = \sum_{i \text{ even}, i \geq 2}^{n_0} K_i \mathbb{E}\{y_m(t)^i\}, \quad (14)$$

where $K_i = \frac{R_{ant}^{i/2}}{i!(\eta_0 v_t)^{i-1}}$. Herein, we focus on the low-power regime, for which it was demonstrated in [6], [19] that truncating the Taylor expansion at $n_0 = 4$ is accurate enough. Therefore, (14) can be written as

$$v_{o,m} = K_2 \mathbb{E}\{y_m(t)^2\} + K_4 \mathbb{E}\{y_m(t)^4\} \quad (15)$$

and the DC power at the m th receiver is given by

$$P_{dc,m} = \frac{v_{o,m}^2}{R_L}, \quad (16)$$

where R_L is the load impedance of the rectifier, while $y_m(t)$ is equal to $y_m^{DMA}(t)$ and $y_m^{FD}(t)$ in the DMA and fully-digital.

E. Power Consumption Model

Lowering the system power consumption is desirable for increasing the end-to-end PTE and this greatly depends on the power consumption of the HPA. Let us denote the maximum efficiency and the maximum output power of a class-B HPA as $\bar{\eta}$ and P_{max} , respectively. Hereby, the efficiency of the i th HPA at time t is expressed as $\eta_i(t) = \bar{\eta} \sqrt{P_{out,i}(t)/P_{max}}$ [32], where $P_{out,i}(t)$ is the output power of the HPA. Then, the corresponding power consumption is

$$P_{hpa,i}(t) = \frac{P_{out,i}(t)}{\eta_i(t)} = \frac{1}{\bar{\eta}} \sqrt{P_{max} P_{out,i}(t)}. \quad (17)$$

Notice that each HPA is in charge of supplying the amount of radiating power by all of the antenna elements, which are fed by its corresponding RF chain. Thus, $P_{out,i}(t)$ is $\sum_{l=1}^{N_h} |x_{i,l}^{DMA}(t)|^2$ in DMA-assisted architecture, and $|x_{i,l}^{FD}(t)|^2$ denotes the output power of the RF chain connected to the l th element in the i th row.

There are also other power consumption sources in the WPT system. For instance, digital baseband power consumption, which is required to perform the digital beamforming, and the RF chain circuit power consumption, including the mixer,

local oscillator, and filter. However, the power consumption of these sources is usually considered fixed and is negligible compared to the HPA. Thus, without loss of generality, the total power consumption of the system is given by

$$P_c = \sum_{i=1}^{N_{rf}} \mathbb{E}\{P_{hpa,i}(t)\} + P_{in}, \quad (18)$$

where $P_{in} = \sum_{i=1}^{N_{rf}} \sum_{n=1}^{N_f} |\omega_{i,n}|^2$ is the total input power.

III. JOINT WAVEFORM & BEAMFORMING OPTIMIZATION

This section formalizes the optimization problem and describes the utilized approach when employing the aforementioned transmit architectures.

A. Problem Formulation

The goal is to obtain a minimum-power waveform and beamforming design to meet the EH requirements of the users. Thus, by utilizing (16) and substituting (17) in (18), the optimization problem can be formulated as

$$\underset{\mathcal{V}}{\text{minimize}} \quad \frac{\sqrt{P_{max}}}{\bar{\eta}} \sum_{i=1}^{N_{rf}} \mathbb{E}\{\sqrt{P_{out,i}(t)}\} + \sum_{i=1}^{N_{rf}} \sum_{n=1}^{N_f} |\omega_{i,n}|^2 \quad (19a)$$

$$\text{subject to} \quad v_{o,m}^2 \geq R_L \bar{P}_m, \quad m = 1, \dots, M, \quad (19b)$$

where \mathcal{V} is the set of optimization variables, which is equal to $\{\omega_{i,n}, q_{i,l}\}_{\forall i,l,n}$ and $\{\omega_{i,n}\}_{\forall i,n}$ for DMA-assisted and fully-digital architectures, respectively. Problem (19) deals with extensive non-linearity since the objective and constraints are highly non-linear and non-convex functions due to the signal model, rectenna non-linearity, and the coupling between the digital and analog beamforming variables in DMA.

B. Optimization Framework for DMA-assisted Architecture

One of the challenges making the problem intractable is the coupling between the optimization variables. To cope with this, we propose using alternating optimization by first optimizing the digital precoders when considering fixed $\{q_{i,l}\}_{\forall i,l}$, followed by optimizing the metamaterial elements' frequency response for fixed $\{\omega_{i,n}\}_{\forall i,n}$.

1) *Optimization with fixed $\{q_{i,l}\}_{\forall i,l}$:* Let us proceed by rewriting the optimization problem as

$$\underset{\{\omega_{i,n}\}_{\forall i,n}}{\text{minimize}} \quad \frac{\sqrt{P_{max}}}{\bar{\eta}} \sum_{i=1}^{N_v} \mathbb{E}\left\{ \sqrt{\sum_{l=1}^{N_h} x_{i,l}^{DMA}(t)^2} \right\} + \sum_{i=1}^{N_v} \sum_{n=1}^{N_f} |\omega_{i,n}|^2 \quad (20a)$$

$$\text{subject to} \quad (K_2 \mathbb{E}\{y_m(t)^2\} + K_4 \mathbb{E}\{y_m(t)^4\})^2 \geq R_L \bar{P}_m, \forall m. \quad (20b)$$

The problem is still highly non-linear and non-convex. Interestingly, it can be easily verified that $v_{o,m}$ is convex and increasing with respect to $y_m(t)^2$, and $y_m(t)$ is affine with respect to $\bar{\mathbf{w}}$. Therefore, $v_{o,m}$ is a convex function with respect to $\bar{\mathbf{w}}$ given a fixed configuration for metamaterial elements [21]. Thus, although (20b) is a non-convex constraint, its left-hand side consists of a convex function. These properties motivate us to adapt the SCA method [33] to optimize the

problem iteratively. Specifically, the objective and constraints can be approximated by their Taylor expansion.

Theorem 1. By defining $S_i = \sum_{l=1}^{N_h} \mathbb{E}\{x_{i,l}^{DMA}(t)^2\}$, we can write

$$\sum_{i=1}^{N_{rf}} \mathbb{E}\left\{\sqrt{\sum_{l=1}^{N_h} x_{i,l}^{DMA}(t)^2}\right\} \leq \sum_{i=1}^{N_{rf}} \tilde{f}(S_i, S_i^{(0)}), \quad (21)$$

where

$$\tilde{f}(S_i, S_i^{(0)}) = \sqrt{S_i^{(0)}} + \frac{1}{2\sqrt{S_i^{(0)}}}(S_i - S_i^{(0)}), \quad \forall i \quad (22)$$

is the first order Taylor expansion of $\sqrt{S_i}$ at point $S_i^{(0)}$.

Proof. The inequality can be proved using Jensen's inequality [34] and the fact that $\sqrt{S_i}$ is a concave function with respect to S_i , while the first-order Taylor expansion of a function is greater than or equal to the function value at each point. \square

Then, we rewrite $v_{o,m}$ considering fixed $q_{i,l}$. For this, we define $\mathbf{a}_{m,n} = \gamma_{m,n} \odot \mathbf{q} \odot \mathbf{h}$ and leverage the fact that the average power of a signal is equal to the power of its spectrum. Thus, we have [6]

$$\mathbb{E}\{y_m(t)^2\} = g_{m,1}(\{\bar{\mathbf{w}}_n\}_{\forall n}) = \frac{G^2}{2} \sum_n |\mathbf{a}_{m,n}^T \bar{\mathbf{w}}_n|^2, \quad (23)$$

$$\mathbb{E}\{y_m(t)^4\} = g_{m,2}(\{\bar{\mathbf{w}}_n\}_{\forall n}) = \frac{3G^4}{8} \sum_{\substack{n_0, n_1, n_2, n_3 \\ n_0 + n_1 = n_2 + n_3}} \dots \quad (24)$$

$$(\mathbf{a}_{m,n_0}^T \bar{\mathbf{w}}_{n_0})(\mathbf{a}_{m,n_1}^T \bar{\mathbf{w}}_{n_1})(\mathbf{a}_{m,n_2}^T \bar{\mathbf{w}}_{n_2})^*(\mathbf{a}_{m,n_3}^T \bar{\mathbf{w}}_{n_3})^*.$$

By leveraging (23) and (24), we can write

$$v_{o,m} \geq K_2 g_{m,1}(\{\bar{\mathbf{w}}_n^{(0)}\}_{\forall n}) + K_4 g_{m,2}(\{\bar{\mathbf{w}}_n^{(0)}\}_{\forall n}) + \sum_n \tilde{g}_{m,n}(\bar{\mathbf{w}}_n^{(0)})(\bar{\mathbf{w}}_n - \bar{\mathbf{w}}_n^{(0)}), \quad (25)$$

where

$$\begin{aligned} \tilde{g}_{m,n}(\bar{\mathbf{w}}_n^{(0)}) &= G^2 K_2 (\mathbf{a}_{m,n}^T \bar{\mathbf{w}}_n^{(0)}) \mathbf{a}_{m,n}^T + \\ &\quad \frac{3K_4 G^4}{8} \left[4 |\mathbf{a}_{m,n}^T|^4 |\bar{\mathbf{w}}_n^{(0)}|^2 \bar{\mathbf{w}}_n^{(0)T} + \right. \\ &\quad \left. 8 \sum_{n_1} |\mathbf{a}_{m,n}^T|^2 |\mathbf{a}_{m,n_1}^T|^2 |\bar{\mathbf{w}}_{n_1}^{(0)}|^2 \bar{\mathbf{w}}_n^{(0)T} + \right. \\ &\quad \left. \sum_{\substack{n_2, n_3 \\ n_2 + n_3 = 2n \\ n_2 \neq n_3}} 2 (\mathbf{a}_{m,n_2}^T \bar{\mathbf{w}}_{n_2}^{(0)})^* (\mathbf{a}_{m,n_3}^T \bar{\mathbf{w}}_{n_3}^{(0)})^* (\mathbf{a}_{m,n}^T \bar{\mathbf{w}}_n^{(0)}) \mathbf{a}_{m,n}^T + \right. \\ &\quad \left. 2 (\mathbf{a}_{m,n_2}^T \bar{\mathbf{w}}_{n_2}^{(0)}) (\mathbf{a}_{m,n_3}^T \bar{\mathbf{w}}_{n_3}^{(0)}) (\mathbf{a}_{m,n}^T \bar{\mathbf{w}}_n^{(0)})^* \mathbf{a}_{m,n}^H + \right. \\ &\quad \left. \sum_{\substack{n_1, n_2, n_3 \\ -n_1 + n_2 + n_3 = n \\ n \neq n_1 \neq n_2 \neq n_3}} 2 (\mathbf{a}_{m,n_1}^T \bar{\mathbf{w}}_{n_1}^{(0)}) (\mathbf{a}_{m,n_2}^T \bar{\mathbf{w}}_{n_2}^{(0)})^* (\mathbf{a}_{m,n_3}^T \bar{\mathbf{w}}_{n_3}^{(0)})^* \mathbf{a}_{m,n}^T + \right. \\ &\quad \left. 2 (\mathbf{a}_{m,n_1}^T \bar{\mathbf{w}}_{n_1}^{(0)}) (\mathbf{a}_{m,n_2}^T \bar{\mathbf{w}}_{n_2}^{(0)}) (\mathbf{a}_{m,n_3}^T \bar{\mathbf{w}}_{n_3}^{(0)})^* \mathbf{a}_{m,n}^H \right] \quad (26) \end{aligned}$$

is the first-order Taylor coefficient of $v_{o,m}$ at point $\{\bar{\mathbf{w}}_n^{(0)}\}_{\forall n}$.

Similarly, it can be verified that

$$\mathbb{E}\{x_{i,l}^{DMA}(t)^2\} = \frac{G^2}{2} \sum_n |q_{i,l} h_{i,l} w_{i,n}|^2. \quad (27)$$

Now, we can reformulate the problem at point $\{\bar{\mathbf{w}}_n^{(0)}, S_i^{(0)}, v_{o,m}\}_{\forall i,n,m}$ as

$$\begin{aligned} \text{minimize} \quad & \frac{\sqrt{P_{max}}}{\bar{\eta}} \sum_{i=1}^{N_{rf}} \tilde{f}(S_i, S_i^{(0)}) + \sum_{i=1}^{N_{rf}} \sum_{n=1}^{N_f} |\omega_{i,n}|^2 \quad (28a) \\ \text{subject to} \quad & \{\bar{\mathbf{w}}_n\}_{\forall n} \\ & \{v_{o,m}\}_{\forall m} \\ & \{S_i\}_{\forall i} \end{aligned}$$

$$\begin{aligned} \text{subject to} \quad & \sqrt{R_L \bar{P}_m} \leq K_2 g_{m,1}(\{\bar{\mathbf{w}}_n^{(0)}\}_{\forall n}) + \\ & K_4 g_{m,2}(\{\bar{\mathbf{w}}_n^{(0)}\}_{\forall n}) + \\ & \sum_n \tilde{g}_{m,n}(\bar{\mathbf{w}}_n^{(0)})(\bar{\mathbf{w}}_n - \bar{\mathbf{w}}_n^{(0)}), \quad \forall m \quad (28b) \end{aligned}$$

$$\frac{G^2}{2} \sum_{n=1}^{N_f} \sum_{l=1}^{N_h} |q_{i,l} h_{i,l} \bar{\mathbf{w}}_n[l]|^2 \leq S_i, \quad i = 1, \dots, N_v, \quad (28c)$$

$$\bar{\mathbf{w}}_n[(i-1)N_h + l] = \bar{\mathbf{w}}_n[l], \quad \forall i, l = 1, \dots, N_h. \quad (28d)$$

Notice that by utilizing (21) and the fact that (20a) consists of two positive terms, one can verify that (28a) serves as an upper bound for (20a), thus, minimizing the latter leads to minimizing the former. Moreover, the inequality in (25) ensures that the solution to this problem is a feasible solution of (20) at each point. Interestingly, the problem² has become convex and can be solved at a given point by standard convex optimization tools, e.g., CVX [35]. Moreover, the solution can be iteratively updated using the SCA algorithm [33].

2) *Optimization with fixed $\{\omega_{i,n}\}_{\forall i,n}$:* Herein, the non-convex Lorentzian constraint of the metamaterials makes the problem extremely difficult to solve. To tackle this, we propose decoupling the problem to first maximize the minimum harvested power when optimizing $q_{i,l}$. This allows us to leverage the beamforming capability of the metamaterial elements and provide degrees of freedom to further reduce the power consumption when optimizing $\omega_{i,n}$ [23]. Hereby, the optimization problem with fixed $\{\omega_{i,n}\}_{\forall i,n}$ can be reformulated as

$$\begin{aligned} \text{maximize} \quad & \min_m \frac{v_{o,m}^2}{R_L} \quad (29a) \\ \text{subject to} \quad & \{q_{i,l}\}_{\forall i,l} \end{aligned}$$

$$\text{subject to} \quad q_{i,l} \in \mathcal{Q}, \quad \forall i, l, \quad (29b)$$

where (29b) is the non-convex Lorentzian constraint. Next, we cope with the complexity caused by the metamaterial elements.

Theorem 2. Problem (29) is equivalent to

$$\begin{aligned} \text{maximize} \quad & R \quad (30a) \\ \text{subject to} \quad & \{q_{i,l}\}_{\forall i,l} \end{aligned}$$

$$\text{subject to} \quad \Re\{q_{i,l}\}^2 + (\Im\{q_{i,l}\} - 0.5)^2 \leq 0.25, \quad \forall i, l, \quad (30b)$$

$$R \leq K_2 E\{y_m(t)^4\} + K_4 E\{y_m(t)^4\}, \quad \forall m. \quad (30c)$$

Proof. The proof is provided in Appendix A. \square

²Note that for the sake of notation and facilitating the reader's understanding, we kept the problem in the vector form and introduced the constraint (28d) into the problem. However, the problem can be easily converted to scalar form, which removes the mentioned constraint.

Algorithm 3 Initialization of digital precoders and the frequency response of the metamaterial elements.

```

1: Input:  $\{\gamma_{i,l,m,n}\}_{\forall i,l,m,n}$ ,  $\tau_s$ ,  $\varsigma$  Output:  $\{\omega_{i,n}, q_{i,l}\}_{\forall i,l,n}$ 
2: Initialize: Compute  $z_m, \forall m$  using (36)
3: Allocate one RF chain to each user,  $\mathcal{R}_m = \{m\}, \forall m$ ,
 $\bar{\mathcal{R}} = \{1, \dots, M\}$ ,  $w_m = 0, \forall m$ 
4:  $N'_v = N_v - M$ ,  $N'_{rf,m} = \lceil z_m N'_v \rceil$ ,  $\mathcal{R}' = \{\}$ 
5: repeat
6:    $m^* = \operatorname{argmax}_{m \notin \mathcal{R}'_m} z_m$ ,  $\mathcal{R}' \leftarrow \mathcal{R}' \cup m^*$ ,  $i_c = M + 1$ 
7:   repeat
8:      $\mathcal{R}_{m^*} \leftarrow \mathcal{R}_{m^*} \cup i_c$ ,  $i_c \leftarrow i_c + 1$ 
9:      $N'_{rf,m} \leftarrow N'_{rf,m} - 1$ ,  $N'_v \leftarrow N'_v - 1$ 
10:    until  $N'_{rf,m} = 0$  or  $N'_v = 0$ 
11:  until  $N'_v = 0$  or  $|\mathcal{R}'| = M$ 
12: for  $m = 1, \dots, M$  do
13:   Compute  $q_{i,l}, \forall i \in \mathcal{R}_m, l$  using (37) and (9),  $w_m = \tau_s$ 
14:   Solve (40) to obtain  $\omega_{i,n}^*$ ,  $\forall i \in \mathcal{R}_m, n$ 
15:   repeat
16:      $\bar{\omega}_{i,n} = w_m, \omega_{i,n} = \bar{\omega}_{i,n} e^{j\bar{\omega}_{i,n}} \forall i \in \mathcal{R}_m, n$ 
17:     Compute  $P_{dc,m}$  using (15), (16), (23), and (24)
18:      $w_m \leftarrow \varsigma w_m$ 
19:   until  $P_{dc,m} \geq \bar{P}_m$ 
20: end for

```

while SCA is used to optimize each set of variables. Each iteration of SCA attempts to solve a quadratic program [33] ((28) or (35)). Moreover, the complexity of quadratic programs scales with a polynomial function of the problem size, while the degree of the polynomial mainly depends on the type of the solver. Let us consider a simple solver based on the Newton method with $\mathcal{O}(n^3)$ complexity [33], where n is the problem size. Imagine U_1 and U_2 are the number of required iterations (in the worst-case) for convergence of digital weights and metamaterial elements' weights, respectively. Furthermore, U_3 is considered the number of iterations required for convergence in alternating optimization. Hereby, the total complexity of the ASCA-DMA algorithm is $\mathcal{O}(U_1 U_2 U_3 n^3)$, where n scales with M , N_v , N_h , and N_f . There is also some additional complexity introduced by the initialization algorithm, which is negligible since the initialization procedure is low-complexity. Moreover, the SCA-FD has only a single SCA stage with a complexity $\mathcal{O}(U_4 n^3)$, where U_4 is the required number of iterations for convergence of SCA in the worst-case.

IV. INITIALIZATION ALGORITHM

Algorithm 3 illustrates the proposed initialization algorithm. Since the initialization algorithm has to be adaptable for multi-user scenarios, we start by proposing a method to allocate the output signal of the RF chains to the different users⁴. For this, we utilize the channel characteristics by naming $n_m^* = \operatorname{argmax}_n |\gamma_{m,n}|$ as the strongest sub-carrier channel between user m and the transmitter. Then, a coefficient z_m is assigned to user m based on the gain introduced by its strongest channel, expressed as

$$z_m = 1 - \frac{|\gamma_{m,n_m^*}|}{\sum_{\bar{m}=1}^M |\gamma_{\bar{m},n_m^*}|}. \quad (36)$$

⁴The allocation is only for the initialization process, and there is no limitation in this regard in the optimization procedure.

More precisely, the RF chains are dedicated to the users based on this ratio such that the users with lower channel gains are served by more signals and vice versa. The allocation procedure is illustrated in lines 2-11 in Algorithm 3. First, an RF chain is allocated to each user, then, the rest of the RF chains are divided among users based on their z_m .

Let us denote \mathcal{R}_m as the set of RF chains dedicated to user m . Then, we initialize $q_{i,l}, i \in \mathcal{R}_m$ to compensate for the phase shift introduced by both $h_{i,l}$ and γ_{i,l,m,n_m^*} . Specifically, we need to define $q_{i,l}, i \in \mathcal{R}_m$ such that

$$\phi_{i,l}^* = \operatorname{argmin}_{\phi_{i,l}} \left\langle \left(\frac{j + e^{j\phi_{i,l}}}{2} \right) h_{i,l} \gamma_{i,l,m,n_m^*} \right\rangle, \forall i, l, \quad (37)$$

where $i \in \mathcal{R}_m$ and $q_{i,l}$ can be obtained accordingly. Notice that (37) can be easily solved using a one-dimensional search with negligible complexity.

The next step is to initialize the amplitude and phase of the digital precoders. For this, let us proceed by defining the received RF power at the m th user as

$$P_{rf,m} = \frac{G^2}{2} |\mathbf{a}_{m,n} \bar{\mathbf{w}}_n|^2 = \frac{G^2}{2} \sum_{n=1}^{N_f} \left| \sum_{i=1}^{N_v} \sum_{l=1}^{N_h} \gamma_{i,l,m,n} q_{i,l} h_{i,l} \omega_{i,n} \right|^2. \quad (38)$$

Moreover, the output DC power of the rectifier is an increasing function of the input RF power when operating in the low-power regime below the breakdown region of the rectifier circuit's diode [36]. Motivated by this, we aim to increase the available RF power at each user during the initialization process using the phases of the digital precoders with low complexity. One way to increase the available RF power for each user is to facilitate the coherent reception of the signals at the receiver. This can be done by reducing the amount of phase shift introduced in the signal. For this, we assume the initial digital weights to be $\omega_{i,n} = \bar{\omega}_{i,n} e^{j\bar{\omega}_{i,n}}$, while the dedicated signals to each user have the same amplitude $\bar{\omega}_{i,n} = w_m, \forall i \in \mathcal{R}_m, n$. Moreover, the ideal phase initialization for maximizing the received RF power is obtained by solving

$$\operatorname{argmax}_{\omega_{i,n} \in [0, 2\pi], \forall i \in \mathcal{R}_m, n} \left| \sum_{n=1}^{N_f} \sum_{i=1}^{N_v} \sum_{l=1}^{N_h} \gamma_{i,l,m,n} q_{i,l} h_{i,l} \bar{\omega}_{i,n} e^{j\bar{\omega}_{i,n}} \right|^2. \quad (39)$$

Meanwhile, solving this problem is not straightforward and introduces much additional complexity to our framework. Notably, the problem can be decoupled and solved individually for each sub-carrier without any change in the optimal solution. Still, there is a coupling between the digital weights of different RF chains in a similar sub-carrier. For this, we further reduce the complexity by formulating the problem as

$$\operatorname{argmin}_{\bar{\omega}_{i,n} \in [0, 2\pi]} \left| \sum_{l=1}^{N_h} \gamma_{i,l,m,n} q_{i,l} h_{i,l} e^{j\bar{\omega}_{i,n}} \right|, \forall i \in \mathcal{R}_m, n. \quad (40)$$

Although the reformulated problem may not have the same solution as (39), it attempts to reduce the total amount of the phase shift of the received signal. Therefore, solving (40) can lead to a suboptimal solution to (39) with much lower complexity, and by using a one-dimensional search. Note that utilizing such an approach is relevant since the goal is

to have a reasonable initialization for the variables, which leads to feeding a feasible initial point to the optimization algorithm. The initialization procedure is illustrated through lines 12-20 in Algorithm 3. For each user, the metamaterials connected to its dedicated RF chains are initialized. Then, the phases of the corresponding digital precoders are obtained. Finally, the amplitudes are iteratively increased until the EH requirement is met and a feasible solution is found. In the fully-digital architecture, the initialization algorithm follows the same procedure with one difference, i.e., each antenna element has a dedicated RF chain, and thus, a dedicated signal.

V. NUMERICAL ANALYSIS

In this section, we provide numerical analysis of the system performance. We consider an indoor office with a transmitter located at the center of the ceiling. The operating frequency of the system is $f_1 = 5.18$ GHz, which matches the characteristics of the utilized rectifier model [36]. The spacing between the elements in the DMA is $\lambda_1/5$, while $\lambda_1/2$ is the distance between two consecutive microstrips. Meanwhile, the inter-element distance is $\lambda_1/2$ in the fully-digital architecture. Thus, $N_v = N_h = \lfloor \frac{L}{\lambda_1/2} \rfloor$ for the fully-digital system, and $N_v = \lfloor \frac{L}{\lambda_1/2} \rfloor, N_h = \lfloor \frac{L}{\lambda_1/5} \rfloor$ for the DMA-assisted system [27]. Note that L is the array length while the arrays are considered to be square-shaped. We set the optimization parameters $\tau_s = 10^{-3}$, $\zeta = 5$, and $\nu = 10^{-6}$. Without loss of generality, we set $G = 1$ and $\bar{\eta} = \frac{\pi^5}{4}$. Finally, the rectifier parameters are $v_t = 25$ mV and $\eta_0 = 1.05$ [20], [21], [36].

We utilize the characteristics of the @Rogers RO4000 series ceramic laminate to calculate the propagation coefficients of the microstrips. Specifically, we calculate the attenuation and propagation coefficients of a RO4000C LoPro with a thickness of 20.7 mil (0.5258 mm) using the formulation provided in [23], which gives $\alpha = 0.356$ m⁻¹ and $\beta = 202.19$ m⁻¹. Based on the rectifier circuit design and simulations in [36], the rectifier circuit diode enters the breakdown region when the received RF power is approximately 100 μ W for a continuous wave ($N_f = 1$). Moreover, it has been shown that the maximum RF-to-DC conversion efficiency is approximately 20% for the mentioned setup. Hence, we establish a minimum requirement of $\bar{P}_{dc} = 20$ μ W for DC harvested power. In the figures, FD refers to the fully-digital architecture. Moreover, d represents the distance between the user and the center of the transmitter.

Fig. 5 provides the convergence performance of the proposed ASCA-DMA approach by presenting the amount of power consumption at the end of each iteration of alternating optimization. It is seen that the objective value gradually decreases with iterations until convergence, while the number of required iterations for convergence depends on the setup. For instance, it is shown that increasing L , N_f , or M can increase the complexity of the problem leading to more iterations. Fig. 6 provides a detailed algorithm performance by showing all iterations of optimization, including the SCA algorithm for both optimizing metamaterials and digital precoders. It is seen that since the minimum harvested power increases

when optimizing \mathbf{q} , the power consumption increases, while this facilitates decreasing the amount of power consumption when optimizing digital precoders. Therefore, the power consumption decreases gradually at the end of each iteration of the alternating optimization (red arrows) until convergence.

Fig. 7 showcases the power consumption of the system as a function of the antenna length. Note that increasing the L reduces the power consumption since the number of elements and the array aperture increases. This leads to more capability in beam focusing, thus, delivering more power to the devices given the same transmit power. However, the performance comparison between DMA and FD highly depends on the system setup. It is seen that DMA outperforms FD when L and P_{max} are relatively low. Note that the output of each RF chain in DMA has to feed all the corresponding elements, while the amount of power consumption scales with the saturation power of the HPA. Thus, when P_{max} is low, the output power of each RF chain in DMA is multiplied by a small value, leading to potential performance gains compared to FD. However, this is only the case when L is low and the number of RF chains is small. On the other hand, in FD, N_{rf} increases with L at a higher rate compared to DMA. Thus, it is easier to reduce the amount of output power of the HPAs by distributing the required output power among them, leading to lower power consumption compared to DMA. However, the value of L that shifts the favorable architecture from DMA to FD or vice versa depends on P_{max} and the transmit power required for meeting the EH requirements. For instance, when $d = 2.5$ m and $P_{max} = 1$ W, the required transmit power and the power consumption multiplier are both low, leading to a shift in performance with lower L . Meanwhile, when $d = 6.5$ m and $P_{max} = 100$ W, DMA outperforms FD up to a higher value of L compared to the previous case. Meanwhile, when d is small and P_{max} is sufficiently large, FD outperforms DMA over all L values with the performance gap increasing with L . In contrast, when d is relatively large and P_{max} is small, DMA becomes the favorable choice for sufficiently large L .

Our results in Fig. 8 corroborate that increasing N_f reduces P_c . As discussed in Section II-C, this is because the HPAs operate in the linear regime, and higher N_f can leverage the rectifier non-linearity and deliver more DC power to the ERs via waveform optimization. However, as previously mentioned, the preference for DMA or FD highly depends on the system parameters. For instance, when $L = 10$ cm and $P_{max} = 1$ W, both N_{rf} and saturation power have small values, leading to a lower power consumption for DMA compared to FD. The reason is that the multiplier of the HPA output power is low, thus, a lower value is multiplied by the output power of each RF chain in DMA. Combining this with a small L , thus a small N_{rf} for FD, leads to DMA outperforming FD. On the other hand, different parameters and system setups may lead to different performances. For example, it is seen that when L and saturation power are both sufficiently large, the favorable architecture shifts from DMA to FD. The reason is that the number of RF chains is much higher for FD in this case, leading to lower output power for each. Then, combining this with a large value of saturation voltage leads to smaller HPA outputs in FD, thus,

⁵In practice, the HPA output power is larger than the input power because $G > 1$. However, the proposed framework applies to all values of G .

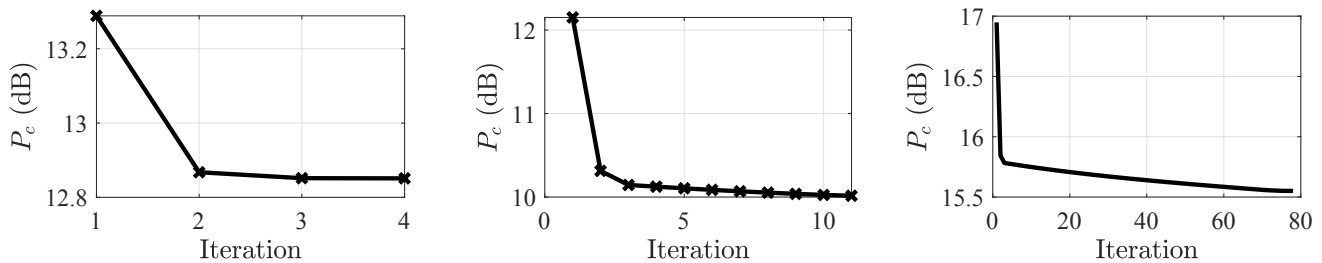


Fig. 5: The convergence performance of ASCA-DMA for (a) $M = 1$, $L = 15$ cm, $N_f = 1$ (left), (b) $M = 1$, $L = 25$ cm, $N_f = 1$ (middle), and (c) $M = 2$, $L = 25$ cm, $N_f = 4$ (right) over iterations with $d = 2.5$ m and $P_{max} = 100$ W.

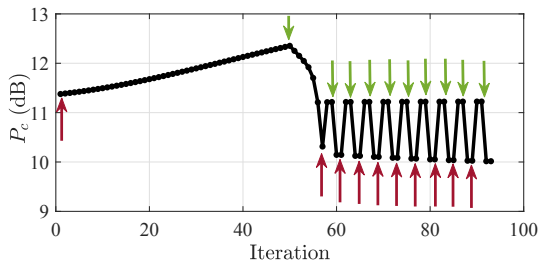


Fig. 6: The convergence performance of ASCA-DMA for $M = 1$, $L = 25$ cm, $d = 2.5$ m, $N_f = 1$, and $P_{max} = 1$ W over all iterations (alternating and SCA). The red and green arrows indicate the starting points of optimization for the metamaterial elements and digital precoders, respectively.

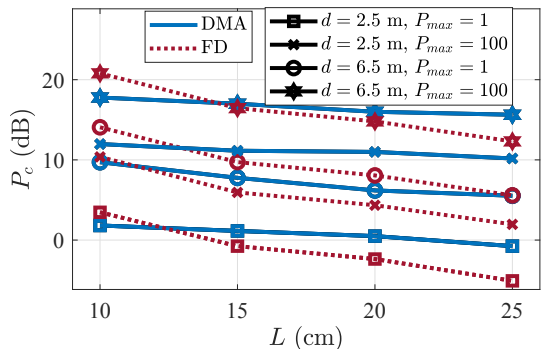


Fig. 7: The power consumption as a function of L for $N_f = 4$, $P_{max} \in \{1, 100\}$ W, and $d \in \{2.5, 6.5\}$ m.

lower power consumption. Meanwhile, increasing N_f affects the performance gap between FD and DMA, and increasing N_f leads to more performance gains in FD compared to DMA since the number of signals is relatively larger in FD. Thus, when DMA outperforms FD for a given L and P_{max} , FD may start outperforming DMA by sufficiently increasing N_f . On the other hand, when FD performs better, increasing N_f can increase the performance gap.

Fig. 9 illustrates the impact of user distance on performance. It is obvious that the power consumption increases with distance since the path loss becomes larger and more transmit power is required to overcome that and meet the EH requirements. Interestingly, the performance shift between FD and DMA is also shown here. It is shown that when both P_{max} and L are relatively low, DMA outperforms FD, especially over large distances. On the other hand, when L increases, DMA starts performing better after a certain d since

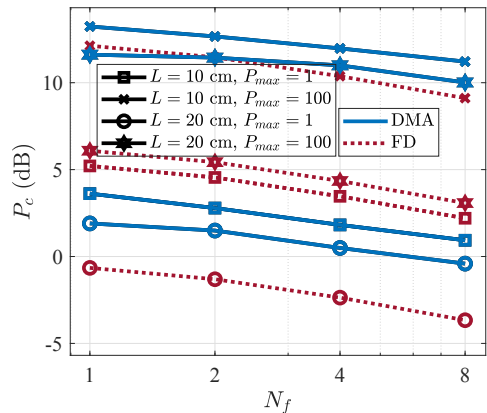


Fig. 8: The power consumption as a function of N_f for $L = 25$ cm, $P_{max} \in \{1, 100\}$ W, $L \in \{10, 20\}$ cm, and $d = 2.5$ m.

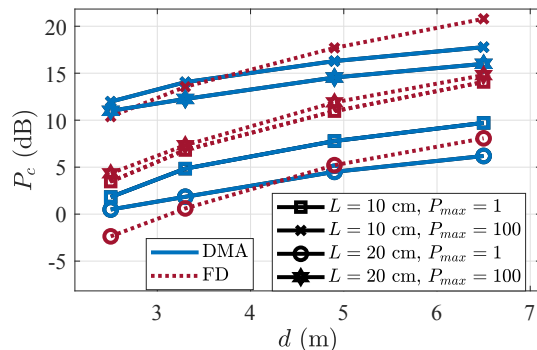


Fig. 9: The power consumption as a function of user distance for $N_f = 4$, $P_{max} \in \{1, 100\}$ W, and $L \in \{10, 20\}$ cm.

the number of HPAs is much larger in FD, and increasing their output power affects the power consumption considerably. For instance, when $L = 20$ cm and $P_{max} = 100$ W, FD starts with better performance than DMA, but the performance gap decreases as d becomes larger.

The impact of the number of users on system performance has been illustrated in Fig. 10 for different system parameters. As expected, the power consumption increases with M since more EH requirements must be met. As previously shown, both DMA or FD may be the favorable choice depending on the system setup and the number of devices. For example, when P_{max} and L are both sufficiently large, DMA outperforms FD for a small M , but FD becomes favorable when M is relatively large. The reason is that increasing M leads to more required transmit power to satisfy the requirements

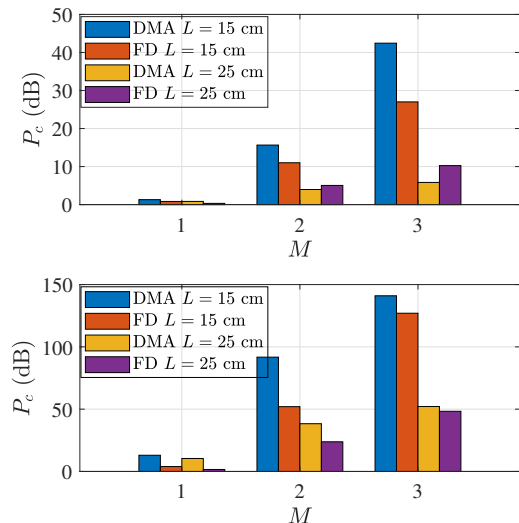


Fig. 10: The power consumption over M for (a) $P_{max} = 1$ W (top) and (b) $P_{max} = 100$ W (bottom), while $N_f = 4$, and $L \in \{15, 25\}$ cm. The users are located at $d = 4.4$ m.

and as earlier mentioned, a large L leads to relatively smaller output powers compared in FD to DMA.

Some discussions on the complexity of implementing a large-scale FD setup are in order. Notice that 36 RF chains are needed in a 400 cm^2 FD array and just 6 for a DMA with the same size at $f_1 = 5.18$ GHz. Thus, although FD may outperform DMA in many setups, as seen earlier, DMA may still be favorable since it can achieve relatively good performance with a reduced N_{rf} and complexity.

Fig. 11 provides some insights regarding the beam focusing capability in the near-field WPT by illustrating the normalized received RF power in each spatial point of the area. Note that the received signal at each point is normalized by its path loss to remove the impact of the distance. In Fig. 11a, it is seen that when the device is located in the near-field region, the beam is focused around the device location, while the beam trace fades increasingly past the device. Such phenomena can have a huge benefit in reducing the RF emission footprint in the environment, which facilitates the implementation of environmentally friendly WPT systems. Meanwhile, the beam pattern for a located device in the far-field is formed in the user's direction, as illustrated in Fig. 11b. This may be highly disadvantaged in interference-sensitive applications since the generated beam may cause difficult-to-handle interference in the signals conveying information, e.g., in SWIPT.

The received RF waveform in DMA-assisted and fully-digital systems is presented in Fig. 12a and Fig. 12b, respectively. As previously mentioned, high PAPR waveforms are beneficial for enhancing the performance in terms of DC harvested power [7]. Moreover, our simulations verify this by showing that the received signal experiences high peak amplitudes at specific intervals. Recall that when HPAs are operating in the linear regime, as in our case, the HPA does not introduce distortion to the signal. Thus, it is beneficial to utilize multiple tones to leverage the rectifier's non-linearity. Note that the peak-to-peak time depends on the characteristics of the EH circuit, mainly the capacitor.

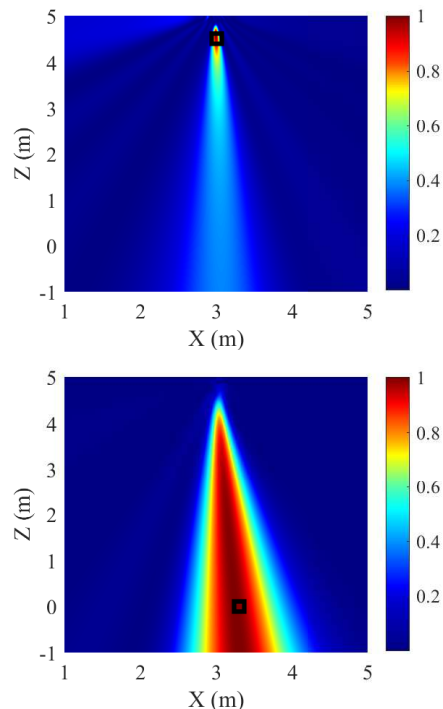


Fig. 11: The normalized received RF power (W) in the area when the energy receiver is located at (a) the near-field region (top) and (b) the far-field region (bottom) in the DMA-assisted system with $L = 30$ cm and $N_f = 1$.

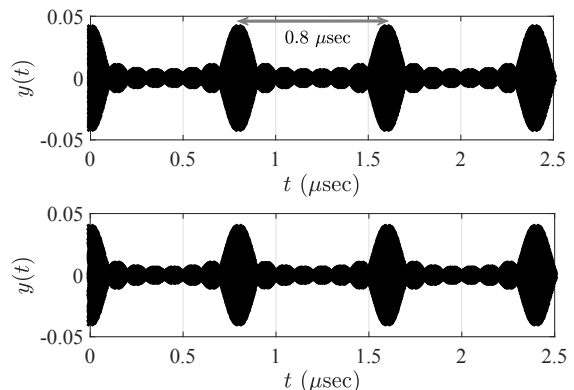


Fig. 12: The received signal at the device using (a) DMA (top) and (b) FD (bottom) for $M = 1$, $L = 25$ cm, and $N_f = 8$.

VI. CONCLUSION AND FUTURE WORK

In this paper, we investigated a multi-antenna near-field WPT system with a DMA as the transmitter to charge multiple non-linear EH devices. Furthermore, we proposed an optimization framework relying on alternating optimization and SCA for the joint waveform optimization and beam focusing to minimize the system power consumption while meeting the EH requirements. Numerical results showed that both DMA and fully-digital architecture may be the favorable choice in terms of power consumption depending on the system setups and parameters such as antenna length, saturation power of the HPAs, number of users, and user distance. Moreover, we showed that increasing the antenna length or the number of tones can enhance the performance. Finally, we verified that the transmitter can focus the energy beams on the spatial points

in the near-field region, while energy beams are formed toward the devices' direction in the far-field.

As a prospect for future research, we may delve deeper into the signal generation aspect by analyzing the power consumption based on the number of tones. Another research direction is to utilize optimization approaches with lower complexity, e.g., relying on machine learning, to learn online the input-output relation of the system's non-linear components while optimizing the transmit waveform accordingly.

APPENDIX

A. Proof of Theorem 2

We relax (29b) by limiting the values of $q_{i,l}$ to lie within the Lorentzian circle in the complex plane. By utilizing the fact that (29a) is a positive and increasing function of the rectifier's output voltage and using the epigraph form, the relaxed problem can be written as (30). Note that each configuration of a metamaterial corresponds to a point on the Lorentzian-constrained circle. Imagine \vec{e} is the vector that represents the direction and gain of a point on the Lorentzian circle, while this direction and gain impacts the transmit signal. Meanwhile, the goal of (30) is to increase the minimum output voltage of the ERs. Therefore, when shaping the transmit signal toward different ERs, it is obvious that \vec{e} should be chosen with the most possible gain in the required direction to improve the signal strength at the receiver. Furthermore, the most possible introduced gain by a metamaterial element along a specified direction happens when the point is exactly on the Lorentzian-constrained circle in that direction. Hence, although (30b) is a relaxed version of the constraint (29b), considering the final solution of the metamaterials as $a\vec{e}$, $0 \leq a \leq 1$, the only solution that leads to the most gain for the desired direction is $a = 1$. Thus, the solution of (30) is the same as (29) leading to a configuration positioned on the Lorentzian circle and the equivalence between the problems.

REFERENCES

- [1] Z. Zhang *et al.*, "6G wireless networks: vision, requirements, architecture, and key technologies," *IEEE Veh. Technol. Mag.*, vol. 14, no. 3, pp. 28–41, 2019.
- [2] N. H. Mahmood *et al.*, "Six key features of machine type communication in 6G," in *2nd 6G SUMMIT*, pp. 1–5, 2020.
- [3] O. L. A. López *et al.*, "High-Power and Safe RF Wireless Charging: Cautious Deployment and Operation," 2023.
- [4] O. L. A. López *et al.*, "Massive wireless energy transfer: enabling sustainable IoT toward 6G era," *IEEE Internet Things J.*, vol. 8, no. 11, pp. 8816–8835, 2021.
- [5] Y. Zeng *et al.*, "Communications and signals design for wireless power transmission," *IEEE Trans Commun.*, vol. 65, no. 5, pp. 2264–2290, 2017.
- [6] B. Clerckx and E. Bayguzina, "Waveform Design for Wireless Power Transfer," *IEEE Trans. Signal Process.*, vol. 64, no. 23, pp. 6313–6328, 2016.
- [7] C. R. Valenta *et al.*, "Theoretical Energy-Conversion Efficiency for Energy-Harvesting Circuits Under Power-Optimized Waveform Excitation," *IEEE Trans. Microw. Theory Tech.*, vol. 63, no. 5, pp. 1758–1767, 2015.
- [8] I. Ahmed *et al.*, "A Survey on Hybrid Beamforming Techniques in 5G: Architecture and System Model Perspectives," *IEEE Commun. Surv. Tutor.*, vol. 20, no. 4, pp. 3060–3097, 2018.
- [9] X. Gao *et al.*, "Energy-Efficient Hybrid Analog and Digital Precoding for MmWave MIMO Systems With Large Antenna Arrays," *IEEE J. Sel. Areas Commun.*, vol. 34, no. 4, pp. 998–1009, 2016.
- [10] Q. Wu *et al.*, "Intelligent Reflecting Surface-Aided Wireless Communications: A Tutorial," *IEEE Trans Commun.*, vol. 69, no. 5, pp. 3313–3351, 2021.
- [11] N. Shlezinger *et al.*, "Dynamic Metasurface Antennas for 6G Extreme Massive MIMO Communications," *IEEE Wirel. Commun.*, vol. 28, no. 2, pp. 106–113, 2021.
- [12] B. Zheng *et al.*, "A Survey on Channel Estimation and Practical Passive Beamforming Design for Intelligent Reflecting Surface Aided Wireless Communications," *IEEE Commun. Surv. Tutor.*, vol. 24, no. 2, pp. 1035–1071, 2022.
- [13] H. Jiang *et al.*, "Hybrid RIS and DMA Assisted Multiuser MIMO Uplink Transmission With Electromagnetic Exposure Constraints," *IEEE J. Sel. Top. Signal Process.*, vol. 16, no. 5, pp. 1055–1069, 2022.
- [14] O. L. A. López *et al.*, "Massive MIMO with radio stripes for indoor wireless energy transfer," *IEEE Trans. Wirel. Commun.*, vol. 21, no. 9, pp. 7088–7104, 2022.
- [15] A. Azarbahram *et al.*, "On the Radio Stripe Deployment for Indoor RF Wireless Power Transfer," 2023.
- [16] O. L. A. López *et al.*, "A Low-Complexity Beamforming Design for Multiuser Wireless Energy Transfer," *IEEE Wireless Commun. Lett.*, vol. 10, no. 1, pp. 58–62, 2021.
- [17] S. Shen and B. Clerckx, "Beamforming Optimization for MIMO Wireless Power Transfer With Nonlinear Energy Harvesting: RF Combining Versus DC Combining," *IEEE Trans. Wirel. Commun.*, vol. 20, no. 1, pp. 199–213, 2021.
- [18] B. Clerckx and E. Bayguzina, "Low-Complexity Adaptive Multisine Waveform Design for Wireless Power Transfer," *IEEE Antennas Wirel. Propag. Lett.*, vol. 16, pp. 2207–2210, 2017.
- [19] Y. Huang and B. Clerckx, "Large-Scale Multiantenna Multisine Wireless Power Transfer," *IEEE Trans. Signal Process.*, vol. 65, no. 21, pp. 5812–5827, 2017.
- [20] S. Shen and B. Clerckx, "Joint Waveform and Beamforming Optimization for MIMO Wireless Power Transfer," *IEEE Trans Commun.*, vol. 69, no. 8, pp. 5441–5455, 2021.
- [21] Y. Zhang and B. Clerckx, "Waveform Design for Wireless Power Transfer With Power Amplifier and Energy Harvester Non-Linearities," *IEEE Trans. Signal Process.*, pp. 1–15, 2023.
- [22] H. Zhang *et al.*, "Near-field wireless power transfer with dynamic metasurface antennas," in *IEEE SPAWC*, pp. 1–5, 2022.
- [23] A. Azarbahram *et al.*, "Energy Beamforming for RF Wireless Power Transfer With Dynamic Metasurface Antennas," *IEEE Wireless Commun. Lett.*, pp. 1–1, 2023.
- [24] O. T. Demir and T. E. Tuncer, "Antenna selection and hybrid beamforming for simultaneous wireless information and power transfer in multi-group multicasting systems," *IEEE Trans. on Wireless Commun.*, vol. 15, no. 10, pp. 6948–6962, 2016.
- [25] Z. Feng *et al.*, "Waveform and Beamforming Design for Intelligent Reflecting Surface Aided Wireless Power Transfer: Single-User and Multi-User Solutions," *IEEE Trans. Wirel. Commun.*, vol. 21, no. 7, pp. 5346–5361, 2022.
- [26] Y. Zhao *et al.*, "RIS-Aided SWIPT: Joint Waveform, Active and Passive Beamforming Design Under Nonlinear Harvester Model," *IEEE Trans Commun.*, vol. 70, no. 2, pp. 1345–1359, 2022.
- [27] H. Zhang *et al.*, "Beam focusing for near-field multiuser MIMO communications," *IEEE Trans. Wirel. Commun.*, vol. 21, no. 9, pp. 7476–7490, 2022.
- [28] S. W. Ellingson, "Path Loss in Reconfigurable Intelligent Surface-Enabled Channels," in *IEEE PIMRC*, pp. 829–835, 2021.
- [29] C. Rapp, "Effects of HPA-nonlinearity on a 4-DPSK/OFDM-signal for a digital sound broadcasting signal," *ESA Special Publication*, vol. 332, pp. 179–184, 1991.
- [30] D. R. Smith *et al.*, "Analysis of a Waveguide-Fed Metasurface Antenna," *Phys. Rev. Appl.*, vol. 8, p. 054048, Nov 2017.
- [31] L. You *et al.*, "Energy Efficiency Maximization of Massive MIMO Communications With Dynamic Metasurface Antennas," *IEEE Trans. Wirel. Commun.*, vol. 22, no. 1, pp. 393–407, 2023.
- [32] C. Lin and G. Y. Li, "Energy-Efficient Design of Indoor mmWave and Sub-THz Systems With Antenna Arrays," *IEEE Trans. Wirel. Commun.*, vol. 15, no. 7, pp. 4660–4672, 2016.
- [33] S. Boyd and L. Vandenberghe, *Convex optimization*. Cambridge university press, 2004.
- [34] E. J. McShane, "Jensen's inequality," 1937.
- [35] M. Grant and S. Boyd, "CVX: Matlab software for disciplined convex programming, version 2.1." <http://cvxr.com/cvx>, Mar. 2014.
- [36] B. Clerckx and J. Kim, "On the beneficial roles of fading and transmit diversity in wireless power transfer with nonlinear energy harvesting," *IEEE Trans. Wirel. Commun.*, vol. 17, no. 11, pp. 7731–7743, 2018.